Supplement of Hydrol. Earth Syst. Sci., 29, 3379–3404, 2025
https://doi.org/10.5194/hess-29-3379-2025-supplement

Hydrology and Earth System Sciences
Open Access
EGU

Supplement of

Evapotranspiration stress intensifies with enhanced sensitivity to soil moisture deficits in a rapidly greening China

Yuan Liu et al.

Correspondence to: Yong Wang (wangyong@iwhr.com)

Supplementary Texts

Text S1. Bayesian Memory Dynamic Linear Model to estimate time-varying sensitivity

We employ the Multivariate Dynamic Linear Model (MDLM) to ascertain the time-varying sensitivities of the ESI with respect to its own lags over the previous 1-5 periods, as well as to various external driving factors. The MDLM, an extension of the Dynamic Linear Model (DLM), comprises both an observation equation and a state evolution equation:

$$y_t = \mathbf{F}_t^T \boldsymbol{\theta}_t + v_t \quad (S1a)$$

$$\boldsymbol{\theta}_t = \boldsymbol{G}\boldsymbol{\theta}_{t-1} + \mathbf{w}_t \quad (S1b)$$

The model disaggregates the ESI time series observations (y_t) into three distinct components: the local/trend (subscript l), seasonal (subscript s), and regression (subscript r) elements. Correspondingly, the regressor vector ($\boldsymbol{F}_t$), state vector ($\boldsymbol{\theta}_t$, representing the sensitivity coefficients), and state evolution matrix ($\boldsymbol{G}$) are each comprised of three analogous components. The observation noise v_t, adheres to a Gaussian distribution with a mean of zero, while the state evolution noise $\mathbf{w}_t$, also conforms to a Gaussian distribution with a mean of zero and is independent from v_t.

$$\boldsymbol{F}_t = \begin{bmatrix} \boldsymbol{F}_l \\ \boldsymbol{F}_s \\ \boldsymbol{F}_{r,t} \end{bmatrix}, \boldsymbol{\theta}_t = \begin{bmatrix} \boldsymbol{\theta}_{l,t} \\ \boldsymbol{\theta}_{s,t} \\ \boldsymbol{\theta}_{r,t} \end{bmatrix}, \boldsymbol{G} = \begin{bmatrix} \boldsymbol{G}_l & 0 & 0 \\ 0 & \boldsymbol{G}_s & 0 \\ 0 & 0 & \boldsymbol{G}_r \end{bmatrix} \quad (S2)$$

The local component is the mean and trend of the ESI, with

$$F_l = \begin{bmatrix} 1 \\ 0 \end{bmatrix}, \theta_{l,t} = \begin{bmatrix} \theta_{l1,t} \\ \theta_{l2,t} \end{bmatrix}, \boldsymbol{G}_l = \begin{bmatrix} 1 & 1 \\ 0 & 1 \end{bmatrix}$$

where $\theta_{l1,t}$ and $\theta_{l2,t}$ indicate the local mean and trend of ESI in the time t, respectively.

The seasonal component comprises a blend of three Fourier series representing seasonality, with frequencies at $\omega_1 = \frac{\pi}{6}, \omega_2 = \frac{\pi}{3}, \text{and} \omega_3 = \frac{2\pi}{3}$,

$$\boldsymbol{F}_s = \begin{bmatrix} \boldsymbol{F}_{s1} \\ \boldsymbol{F}_{s2} \\ \boldsymbol{F}_{s3} \end{bmatrix}, \boldsymbol{\theta}_{s,t} = \begin{bmatrix} \boldsymbol{\theta}_{s1,t} \\ \boldsymbol{\theta}_{s2,t} \\ \boldsymbol{\theta}_{s3,t} \end{bmatrix}, \boldsymbol{G}_s = \begin{bmatrix} \boldsymbol{G}_{s1} & 0 & 0 \\ 0 & \boldsymbol{G}_{s2} & 0 \\ 0 & 0 & \boldsymbol{G}_{s3} \end{bmatrix}$$

where

$$\boldsymbol{F}_{s(i)} = \begin{bmatrix} 1 \\ 0 \end{bmatrix}, \boldsymbol{\theta}_{s(i),t} = \begin{bmatrix} \theta_{s(i),1,t} \\ \theta_{s(i),2,t} \end{bmatrix}, \boldsymbol{G}_{s(i)} = \begin{bmatrix} \cos\ \omega_i & \sin\ \omega_i \\ -\sin\ \omega_i & \cos\ \omega_i \end{bmatrix}, i \in \{1,2,3\}$$

Based on historical data up to time step t, the expected value of the seasonal component at time $t + k$ can be represented by the sum of three cosine functions, each characterized by distinct frequencies, amplitudes, and phases.

$$\begin{aligned} \mathbb{E}\left[y_{s,t+k} \middle| y_{s,1}, \dots, y_{s,t}\right] &= \boldsymbol{F}_s^T \boldsymbol{\theta}_{s,t+k} \\ &= \sum_{i=1}^{3} \boldsymbol{F}_{s(i)}^T \boldsymbol{G}_{s(i)}^k \boldsymbol{\theta}_{s(i),t} \\ &= \sum_{i=1}^{3} \begin{bmatrix} 1 & 0 \end{bmatrix} \begin{bmatrix} \cos \omega_i k & \sin \omega_i k \\ -\sin \omega_i k & \cos \omega_i k \end{bmatrix} \begin{bmatrix} \theta_{s(i),1,t} \\ \theta_{s(i),2,t} \end{bmatrix} \\ &= \sum_{i=1}^{3} A_{i,t} \cos\left(\omega_i k + \phi_{i,t}\right) \end{aligned} \quad (S3)$$

where $A_{i,t}$ and $\phi_{i,t}$ represent the magnitudes and phases of the harmonic components, respectively. Both $A_{i,t}$ and $\phi_{i,t}$ are dictated by $\boldsymbol{\theta}_{s(i),t}$.

The regression component employs a set of independent variables $(x_1, x_2, \dots, x_p)$ to model their impact on the dependent variable y_t.

$$\boldsymbol{F}_{r,t} = [x_{1,t}, x_{2,t}, \dots, x_{p,t}]^T, \boldsymbol{G}_r = \boldsymbol{I}_p$$

where $\boldsymbol{I}_p$ is the identity matrix of dimension p. The set of independent variables comprises the deseasonalized and detrended anomalies of the ESI from the preceding five time periods (Lag1~Lag5), as well as the anomalies of the driving factors for the current time step. These deseasonalized and detrended ESI anomalies are derived by applying a DLM devoid of regression elements, effectively eliminating the trend and seasonal fluctuations from the ESI time series. The terms Lag1~Lag5 refer to the cumulative average of the respective preceding time periods. Specifically,

Lag1 corresponds to the immediate prior interval, encompassing the past 8 days; Lag2 covers the time span from 8 to 16 days prior, exclusive of Lag1; and so forth. Consideration is limited to Lag1 through Lag5 because the impact of more distant time periods is deemed sufficiently minimal to warrant exclusion.

To address the aforementioned MDLM, we employed a technique known as forward filtering. This approach is conceptually akin to Kalman Filtering but incorporates an extra step to retroactively refine the posterior estimate of y_t in order to derive the posterior estimate of $\boldsymbol{\theta}_t$. Initially, we presuppose that the variances of the noise components v_t and $\mathbf{w}_t$ are predetermined.

(1) Posterior at $t-1$. Given all observations $D_{t-1} = \{y_1, y_2, \dots, y_{t-1}\}$, $\boldsymbol{\theta}_{t-1}$is assumed to follow a multivariate normal distribution:

$$\boldsymbol{\theta}_{t-1}|D_{t-1} \sim N(\boldsymbol{m}_{t-1}, \boldsymbol{C}_{t-1}) \quad (S4)$$

where $\boldsymbol{m}_{t-1}$ is the predicted mean, and $\boldsymbol{C}_{t-1}$ is the variance matrix.

(2) Prior at t. Together with Eq. 2, we can get the prior distribution of $\boldsymbol{\theta}_t$,

$$\boldsymbol{\theta}_t|D_{t-1} \sim N(\boldsymbol{a}_t, \boldsymbol{R}_t) \quad (S5)$$

where

$$\boldsymbol{a}_t = \boldsymbol{G}_t\boldsymbol{m}_{t-1}, \boldsymbol{R}_t = \boldsymbol{G}_t\boldsymbol{C}_{t-1}\boldsymbol{G}_t^T + \boldsymbol{W}_t$$

(3) One step forecast. Together with Eq. 1, the predictive distribution of y_t is

$$y_t|D_{t-1} \sim N(f_t, q_t) \quad (S6)$$

where

$$f_t = \boldsymbol{F}_t^T\boldsymbol{a}_t, q_t = \boldsymbol{F}_t^T\boldsymbol{R}_t\boldsymbol{F}_t + v_t$$

(4) Posterior at t. Compared with the observed y_t, the posterior estimate of $\boldsymbol{\theta}_t$ based on all observations up to time t is derived using Bayes' rule:

$$p(\boldsymbol{\theta}_t|D_t) = p(\boldsymbol{\theta}_t|y_t, D_{t-1}) \propto p(\boldsymbol{\theta}_t|y_t, D_{t-1})p(y_t|\boldsymbol{\theta}_t, D_{t-1}) = N(\boldsymbol{m}_t, \boldsymbol{C}_t) \quad (S7)$$

with

$$\boldsymbol{m}_t = \boldsymbol{a}_t + \boldsymbol{A}_t e_t, \boldsymbol{C}_t = \boldsymbol{R}_t - q_t\boldsymbol{A}_t\boldsymbol{A}_t^T$$

where

$$e_t = y_t - f_t, \boldsymbol{A}_t = \boldsymbol{R}_t\boldsymbol{F}_t/q_t$$

Here, $\boldsymbol{A}_t$ is the matrix of adaptive coefficients, e_t represents the one-step forecast errors. When y_t is missing due to cloud or snow, the prior from historical data $p(\boldsymbol{\theta}_t|D_{t-1})$ from Eq. 4 is used to estimate $\boldsymbol{\theta}_t$.

In practice, the variance of noise v and $\boldsymbol{W}_t$ are unknown. Consequently, we have refined the process for variance estimation. Initially, we posit that $v_t \sim N(0, v)$ and $\boldsymbol{w}_t \sim N(0, v\boldsymbol{W}_t^*)$. Both v and $\boldsymbol{W}_t^*$ are unknown parameters, with $\boldsymbol{W}_t^*$ being a rescaled version of $\boldsymbol{W}_t$. Given v, Eqs. 4-7 adheres to a consistent format,

$$\boldsymbol{\theta}_{t-1}|D_{t-1}, v \sim N(\boldsymbol{m}_{t-1}, v\boldsymbol{C}_{t-1}^*) \quad (S8)$$
$$\boldsymbol{\theta}_t|D_{t-1}, v \sim N(\boldsymbol{a}_t, v\boldsymbol{R}_t^*) \quad (S9)$$
$$y_t|D_{t-1}, v \sim N(f_t, vq_t^*) \quad (S10)$$
$$\boldsymbol{\theta}_t|D_t, v \sim N(\boldsymbol{m}_t, vC_t^*) \quad (S11)$$

We assume the variation of observational error (v) follows an inverse-gamma (IG) distribution,

$$v|D_{t-1} \sim IG(n_{t-1}/2, d_{t-1}/2) \quad (S12)$$
$$v|D_t \sim IG(n_t/2, d_t/2) \quad (S13)$$
$$n_t = n_{t-1} + 1$$
$$d_t = d_{t-1} + e_t^2/q_t^*$$

where n_t is the degree of freedom, and

$$\boldsymbol{\theta}_{t-1}|D_{t-1} \sim T(\boldsymbol{m}_{t-1}, s_{t-1}\boldsymbol{C}_{t-1}^*) \quad (S14)$$
$$\boldsymbol{\theta}_t|D_{t-1} \sim T(\boldsymbol{a}_t, s_{t-1}\boldsymbol{R}_t^*) \quad (S15)$$
$$y_t|D_{t-1} \sim T(f_t, s_{t-1}q_t^*) \quad (S16)$$
$$\boldsymbol{\theta}_t|D_t \sim T(\boldsymbol{m}_t, s_t\boldsymbol{C}_t^*) \quad (S17)$$
$$s_{t-1} = d_{t-1}/n_t$$
$$s_t = d_t/n_t$$

We estimate $\boldsymbol{W}_t$ using a discounting approach. Based on Eq. 5, the prior variance of $\boldsymbol{\theta}_t$ as $Var(\boldsymbol{\theta}_t| = D_{t-1}) = \boldsymbol{R}_t = \boldsymbol{G}_t\boldsymbol{C}_{t-1}\boldsymbol{G}_t^T + \boldsymbol{W}_t = \boldsymbol{P}_t + \boldsymbol{W}_t$, where $\boldsymbol{P}_t$ is the variance without stochastic noise, that is, $\boldsymbol{W}_t = 0$. If $\boldsymbol{W}_t \neq 0$, we assert that $\boldsymbol{R}_t = \boldsymbol{P}_t/\delta$, with the parameter $\delta \in (0,1]$. This indicates that stochastic noise leads to an inflation of the variance by a factor of $\frac{1}{\delta} - 1$ at each step, correspondingly diminishing the degrees of freedom from n_t to δn_t. Consequently, a smaller δ incurs more significant fluctuations in $\boldsymbol{\theta}_t$, and the inverse is true. To ensure the stability of local trends and seasonal components, minimally influenced by anomalies, we employ diverse δ values, selected through a grid search algorithm from the set [0.97,0.98,0.99,0.995,0.999]. We initialize the model at time step 0

using non-informative priors $\boldsymbol{m}_0 = 0, \boldsymbol{C}_0 = \boldsymbol{I}, n_0 = p, d_0 = 0.2^2 n_0$, permitting the parameter $\boldsymbol{\theta}_t$ to fluctuate freely initially and then gradually converge with the accumulation of more observations. To mitigate the effects of the initial substantial fluctuation and facilitate a gradual convergence of variance, we employ the first five years of ESI and drivers' data twice in a preparatory phase known as the "spin-up" period.

The model parsing process, influenced by Bayesian updating and Markov assumptions, introduces error terms and noise, necessitating the optimization of the δ value(Simoen et al., 2013; Zhang et al., 2011). For each pixel, the original sequence is partitioned into a training set and a validation set with an 80:20 ratio. Subsequently, we compute the coefficient of determination (R^2), root mean square error (RMSE), and mean absolute error (MAE) by comparing the original ESI sequence with the aggregate of the three components post-MDLM decomposition for both segments. This approach facilitates the evaluation of MDLM's precision in deconstructing and tracking the influence and reaction of evolving environmental conditions on evaporation stress (Fig. S10 for verification results).

Supplementary Figures

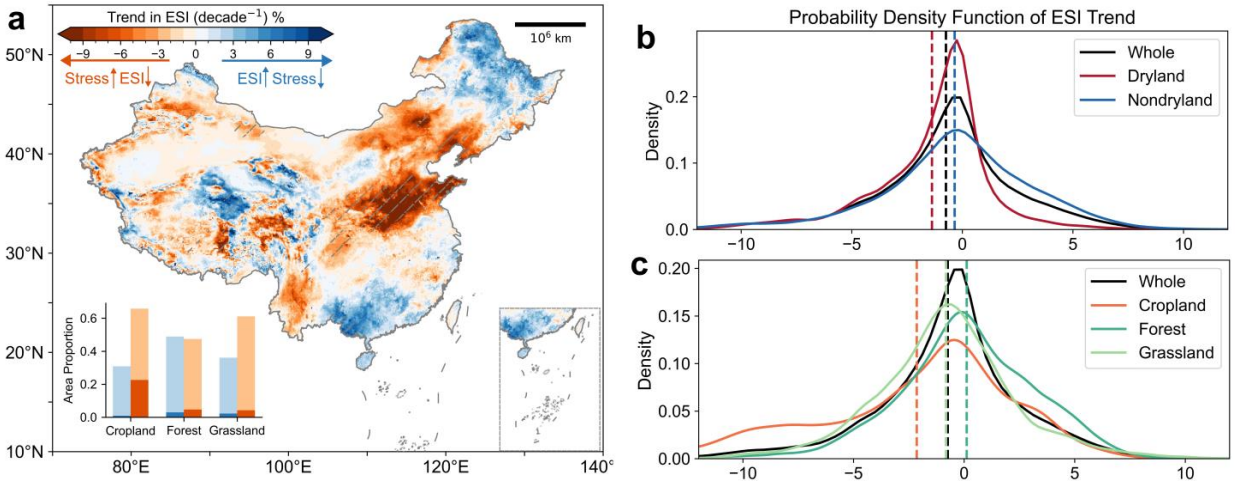

Figure S1. Spatial distribution of the tendency in ESI over the past 20 years. Same as Figs. 3cde in the main text, but ESI is calculated based on ETp that takes into account the CO_2 effect, with the time span from 2001 to 2020.

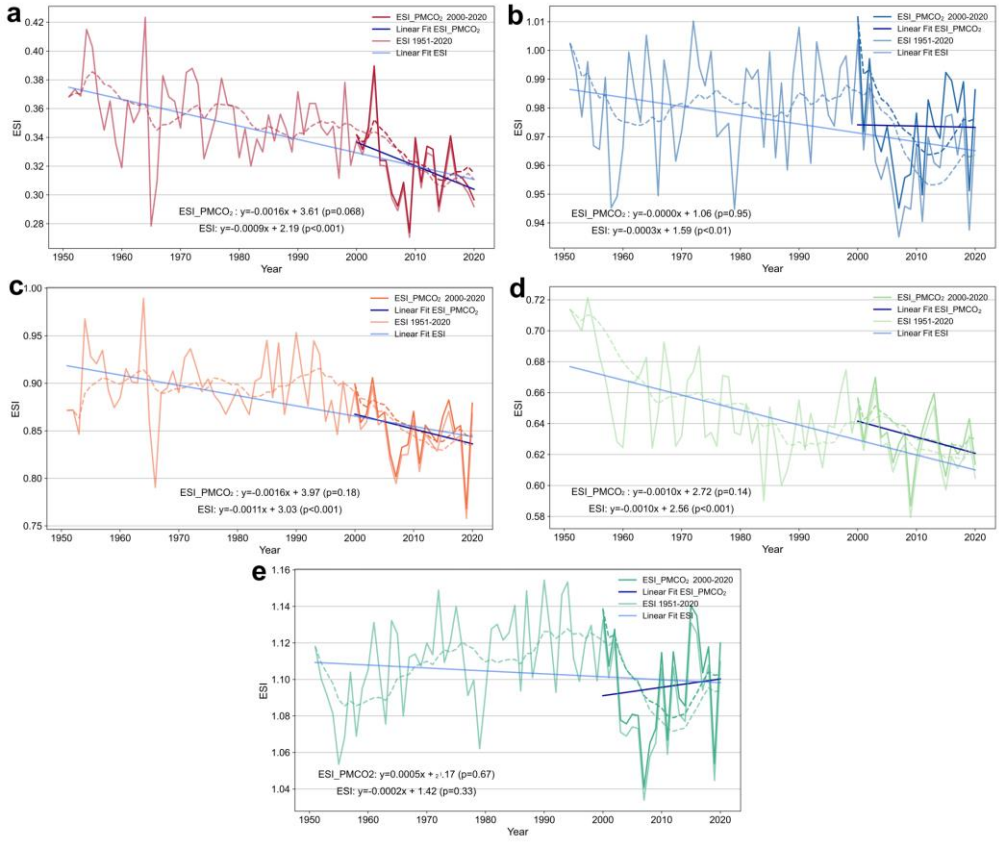

Figure S2. Time series and linear fitting of the regional average ESI. Same as Fig. 3a, but here it is for different climate zones and land use types, where (a) is dryland, (b) is non-dryland, (c) is cropland, (d) is grassland, and (e) is forest.

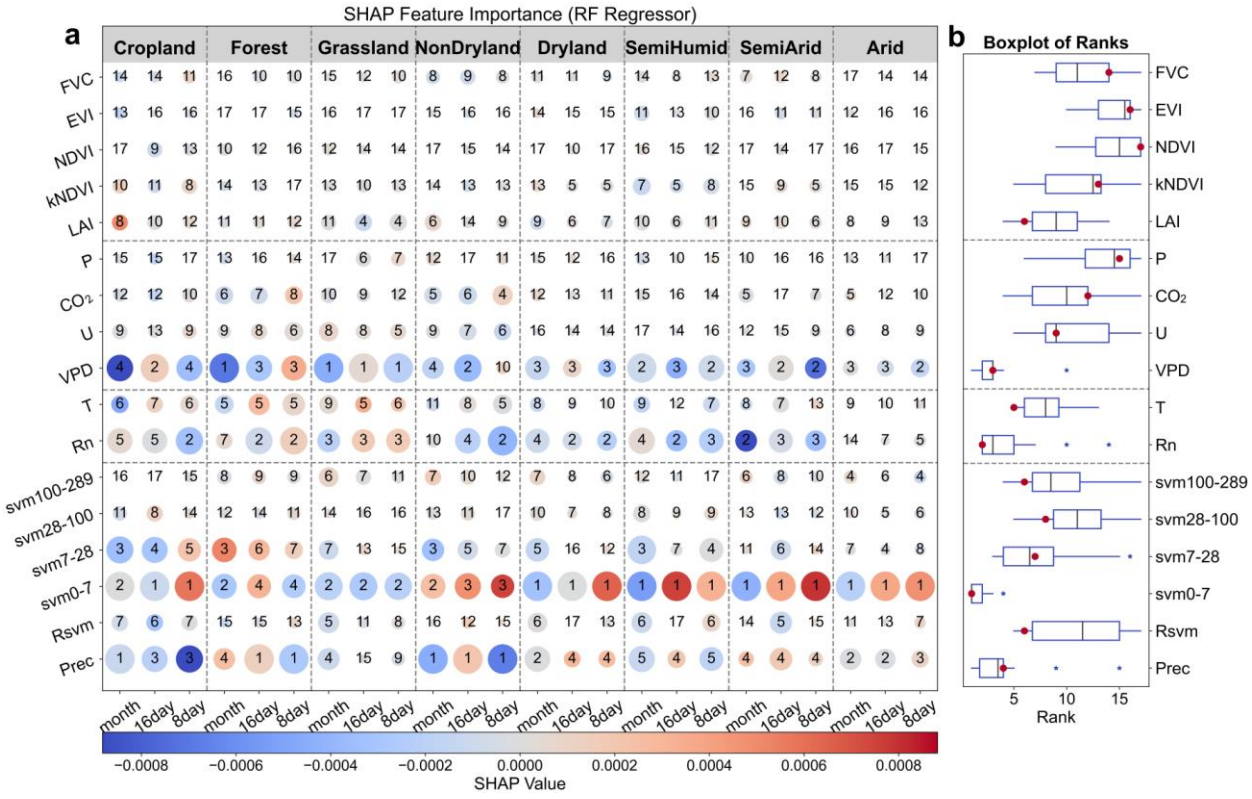

Figure S3. Identification of the key external drivers of ESI. Same as Fig. 4, but applying the RF regressor. It is consistent with the overall results identified by the XGBoost classifier, except that it fails to distinctly differentiate between surface soil moisture and precipitation.

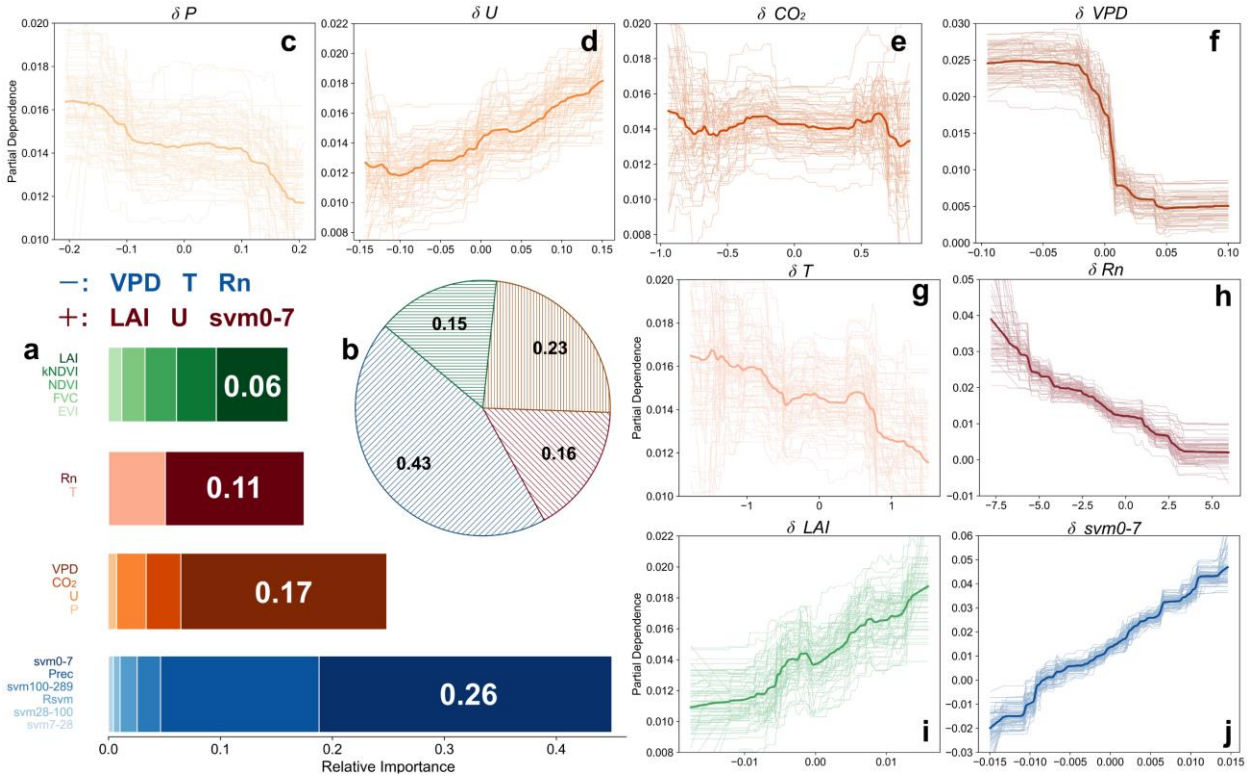

Figure S4. Importance and partial dependence of external drivers influencing ESI. Same as Fig. 5, but here examines the 16-day temporal resolution. The hierarchy of importance is as follows: water, climate, energy, and then vegetation. Compared to the 8-day temporal resolution findings, the importance of water and vegetation factors remains virtually unchanged, with svm0-7, VPD, Rn and LAI as the most influential variables within their respective categories.

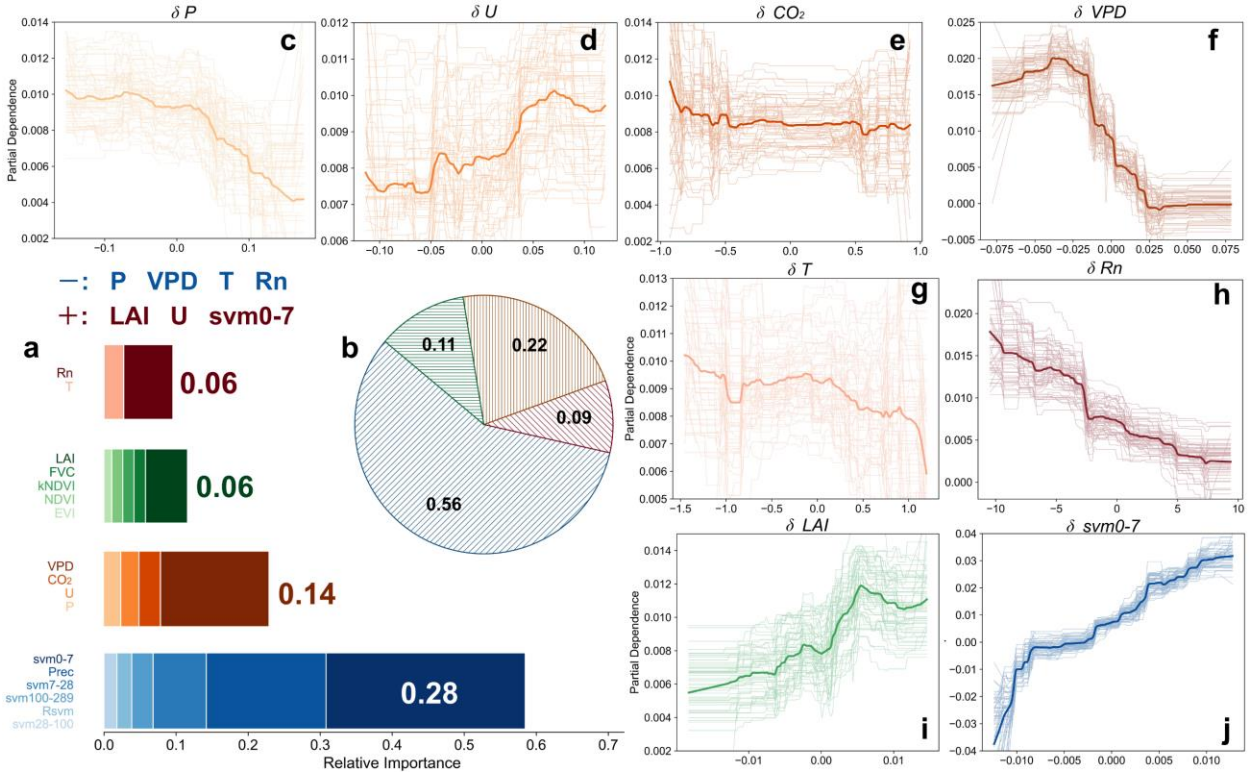

Figure S5. Importance and partial dependence of external drivers influencing ESI. Same as Fig. 5 & S4, but here analyze monthly series data. The order of importance is water > climate > vegetation > energy. Compared to the results from the 8-day and 16-day temporal results, the significance of water is amplified (with an increase to 0.56), whereas the contributions of vegetation and energy factors are diminished, with the latter being particularly affected. Factors such as svm0-7, VPD, LAI, and Rn continue to be the most influential within their respective categories, aligning with observations from the other temporal scale. The dependency direction of the pivotal factor aligns with that of the other two temporal dimensions.

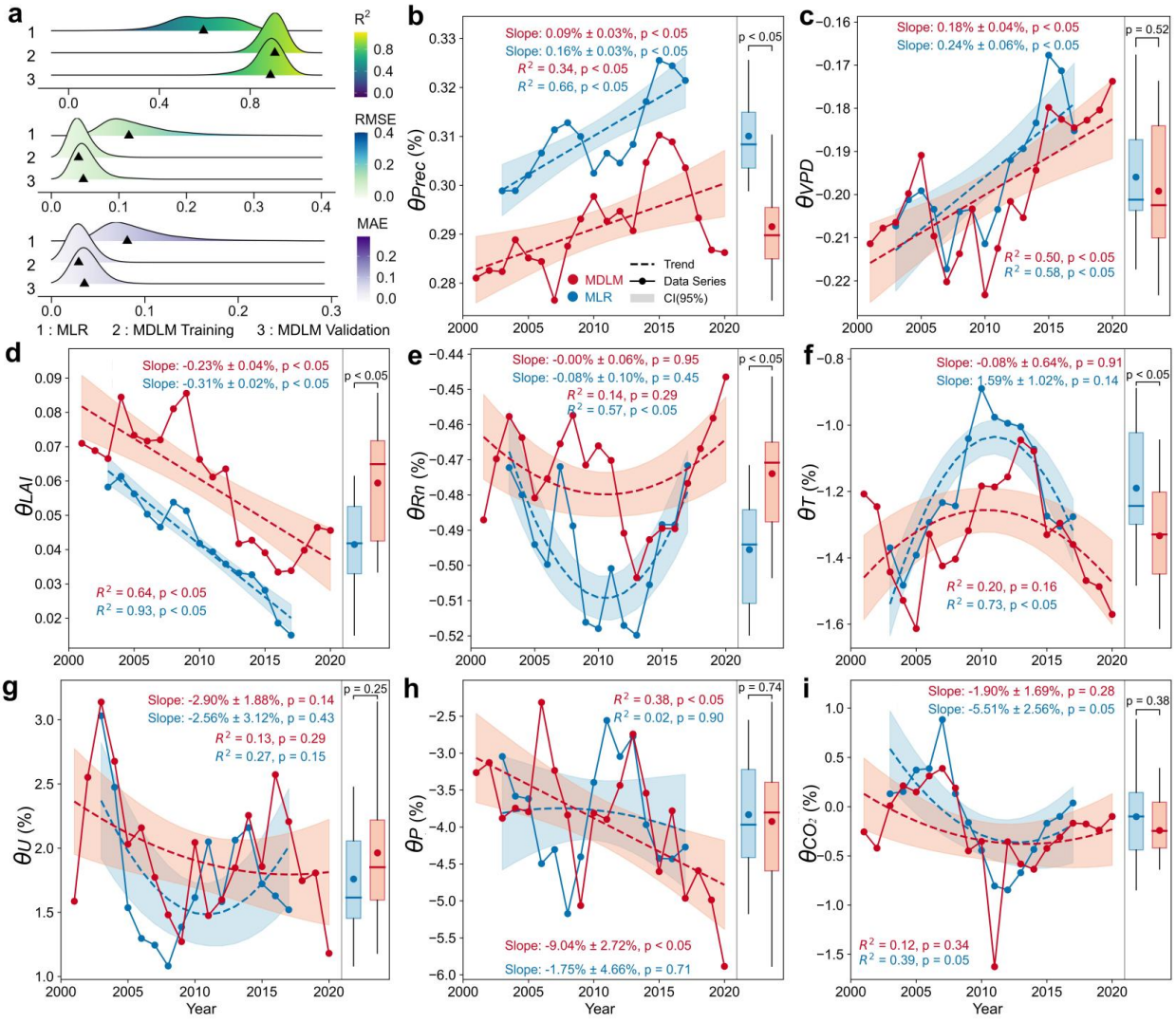

Figure S6. Sensitivity of the ESI to pivotal external drivers and its dynamic trajectory. Same as Fig. 6, but here the models establish the sensitivity profile for the following external factors: Precipitation -Prec, Rn, T, VPD, U, CO_2, and LAI (Parameter Set: R1). In Figure a, the MDLM model demonstrated significantly higher accuracy in both the training and validation sets compared to MLR. The sequences of Prec, VPD, LAI, Rn, and T derived from the two models exhibited substantial differences, highlighting the MDLM model's notable improvement in predicting key variables. Except for Rn, the sensitivity of additional factors displayed a consistent pattern in both magnitude and directional trend. The observed trend of key factors aligns with the R0 scenario that corroborates the robustness of research findings. These findings indicate heightened sensitivity to both water supply and VPD, coupled with a diminished sensitivity of LAI.

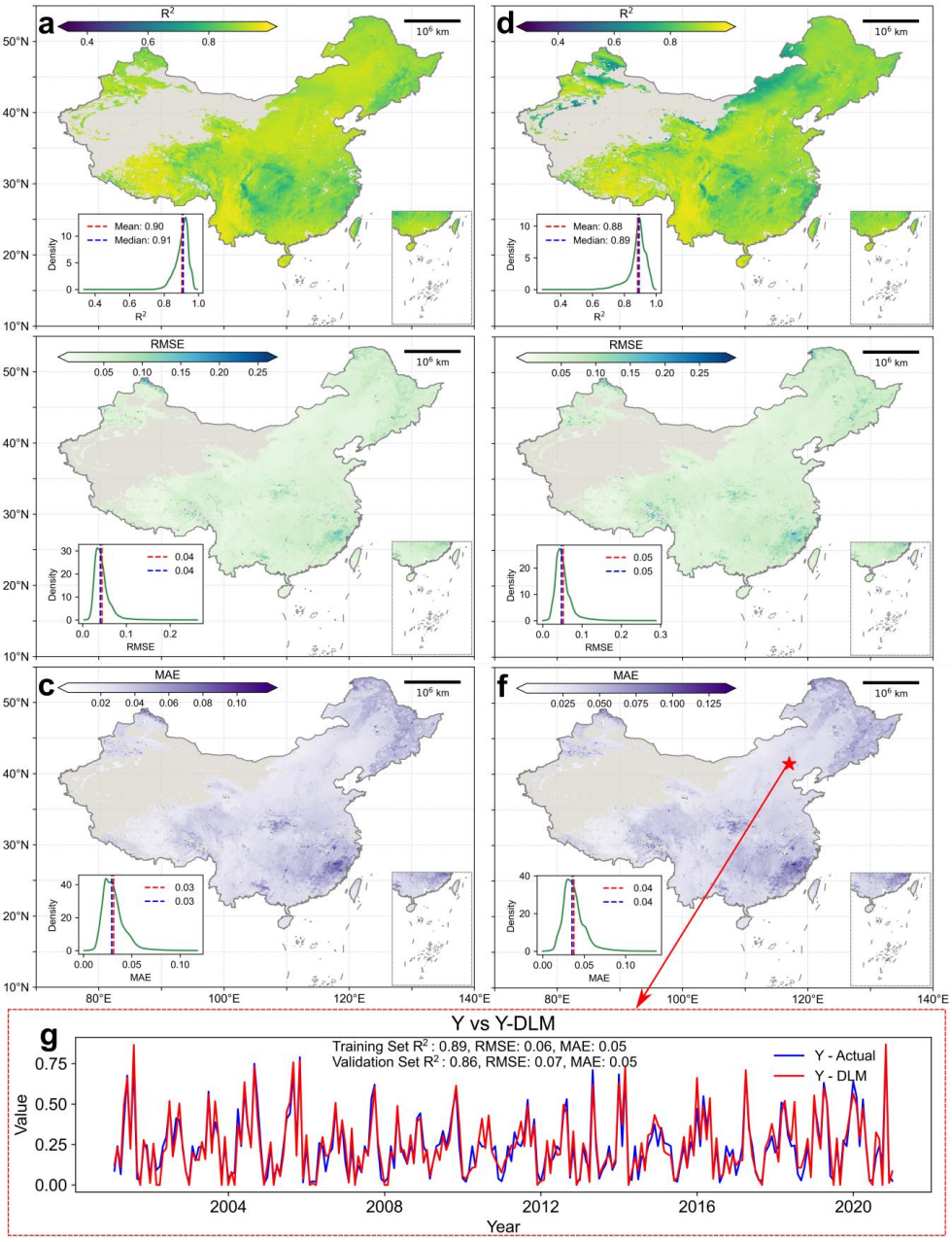

Figure S7. Simulation accuracy and validation of the MDLM model. For each pixel, the dataset was partitioned into a training set and a validation set at a ratio of 8:2, facilitating the evaluation of the model's ability to accurately fit the actual ESI sequence, along with its local, seasonal, and trend components. This process is exemplified through the analysis of a single pixel in (g), with the method detailed in Text S1. (a-c) The distribution of the R^2, RMSE, and MAE for the training set, with R0 parameter set. These figures include insets that show the distributions across the region, with the mean and median values delineated by red and green dashed lines, respectively. (d-f) The model's performance for the validation set. The analyses reveal that the MDLM model achieves a consistently high fitting accuracy, evidenced by an average R^2 of 0.88, an RMSE of 0.04, and an MAE of 0.03. It is noted that results exhibit suboptimal performance in certain areas of the southeastern region, however, remain relatively high credibility in other areas.

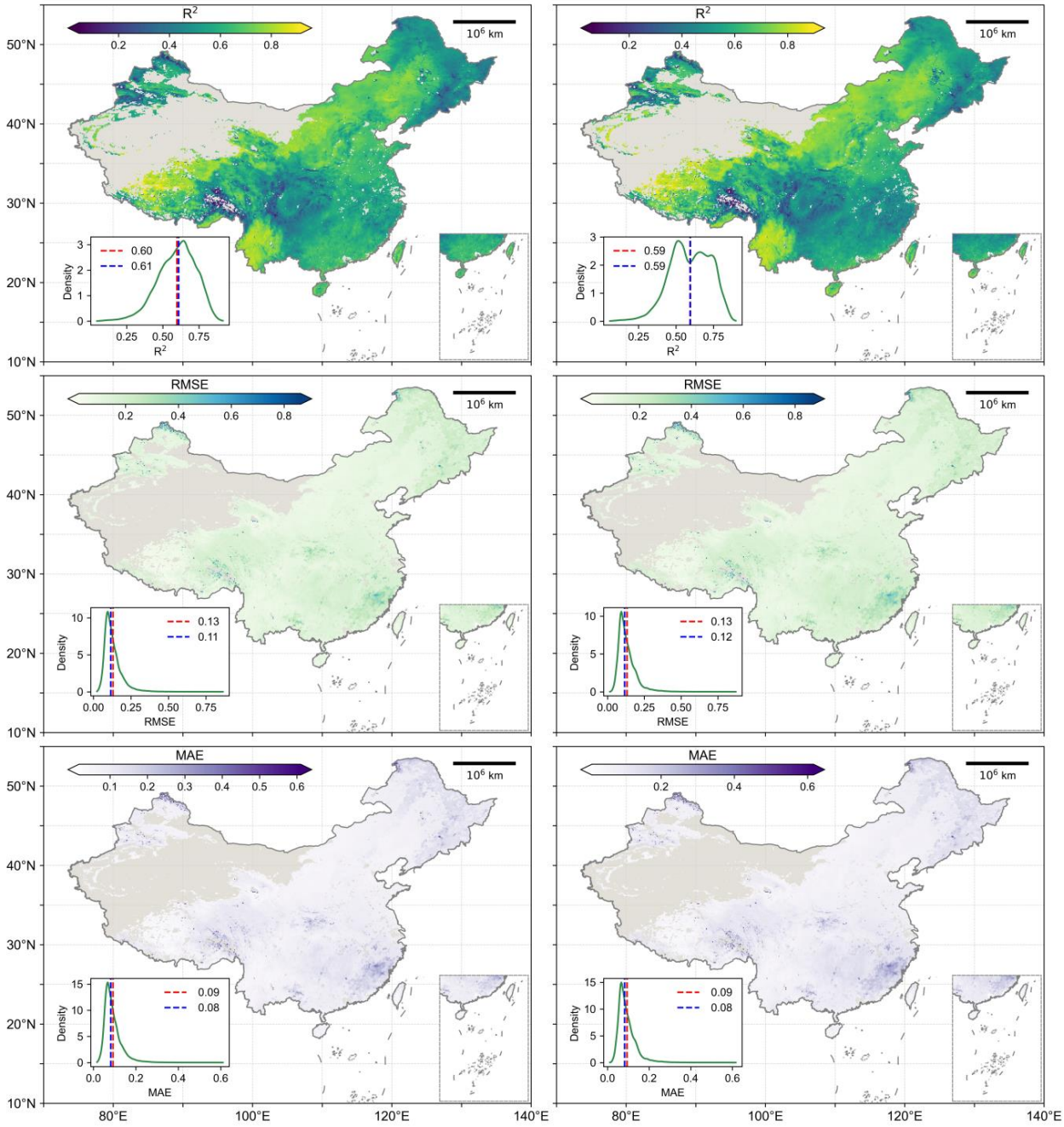

Figure S8. Simulation accuracy and validation of the MLR model. (a-c) The distribution of the R^2, RMSE, and MAE for model with Parameter Set R0. The model achieved an average R^2 of 0.60, RMSE of 0.13, and MAE of 0.09 across the entire region**.** (d-f) The model's performance using the Parameter Set R1, with an average R^2 of 0.59, RMSE of 0.13, and MAE of 0.09 across the entire region.

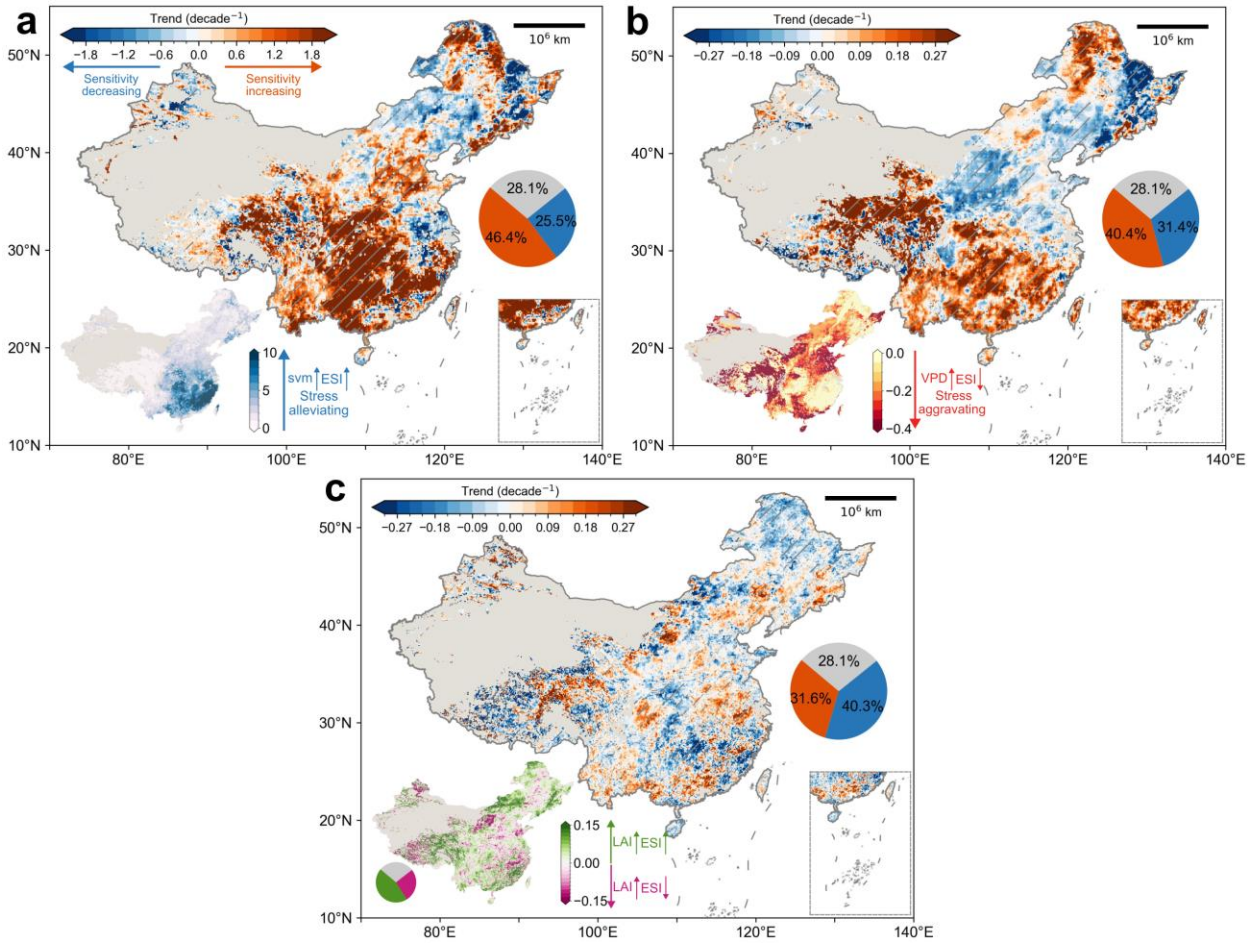

Figure S9. Spatiotemporal heterogeneity in svm0-7, VPD, and LAI sensitivity. Same as Fig. 7a-c, but the sensitivity is derived from the MLR model with the external driving factors input (R0): svm0-7, Rn, T, VPD, U, CO_2, and LAI. Given that the MLR model generates an averaged sensitivity series within a 5-year moving window, and the MLDM produces time-specific sequences, the figure is not numerically comparable to Figure 8. Instead, it serves to contrast the spatial distribution patterns and relative magnitudes across different categories. The patterns for $\boldsymbol{\theta_{svm}}$ $\boldsymbol{\theta_{VPD}}$ and $\boldsymbol{\theta_{LAI}}$ depicted in figures (a-f) are consistent with Fig. 7, with similar area proportions, affirming the results' robustness. Here, the same color scheme as Fig. 7 (a-f) is used, which also reveals the MLR model's significant overestimation of sensitivity trend.

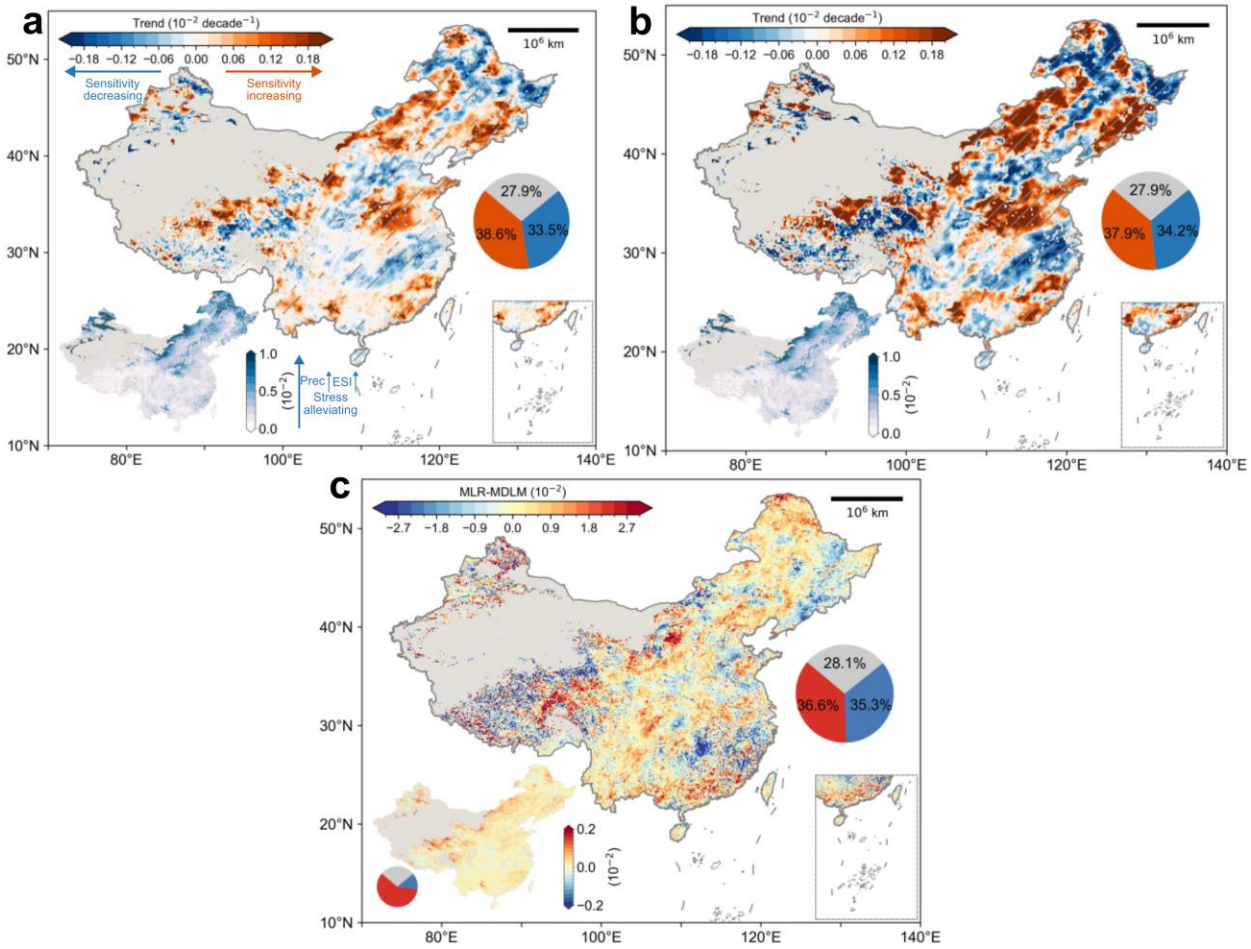

Figure S10. Spatiotemporal heterogeneity in sensitivity of ESI to Prec. Same as Fig. 9a，Fig. S9a and Fig. 9d, but the sensitivity is derived from the MDLM（a） and MLR（b） model with the external driving factors input (R1): Prec, Rn, T, VPD, U, CO_2, and LAI. The main figure displays the spatial distribution of the Sen's slope for $\boldsymbol{\theta_{Prec}}$, whereas the inset presents the spatial distribution of the multi-year average of $\boldsymbol{\theta_{Prec}}$. Figure (c) delineates the differences between (a) and (b). This figure further corroborates the analogous patterns in the simulation outcomes of the two models, along with the MLR model's overestimation of the intensity of change trends, where both positive and negative trends are more pronounced.

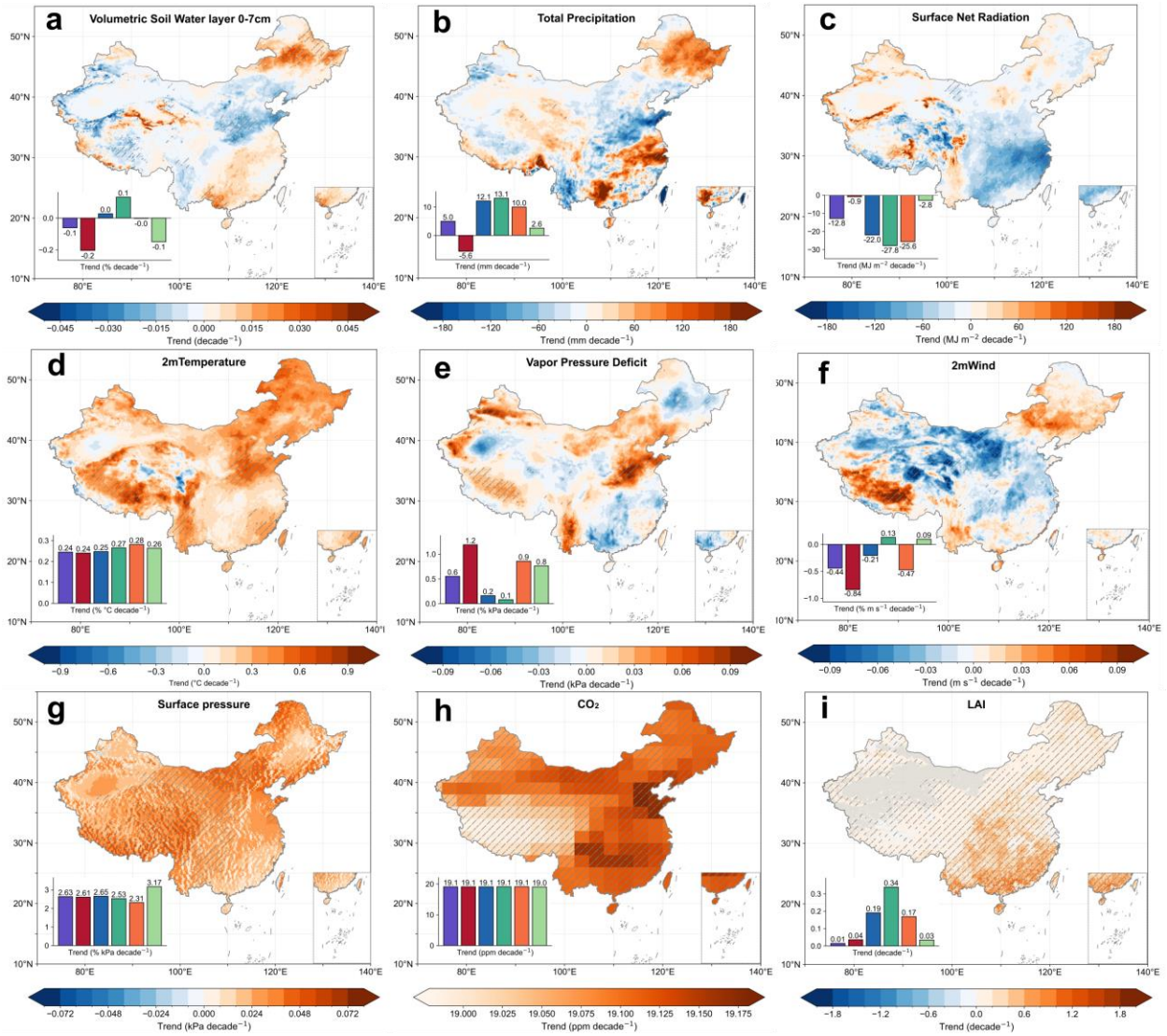

Figure S11. Spatiotemporal patterns of regional hydrological, meteorological, and vegetation variables over the period from 2001 to 2020. (a) Surface soil water at 0-7 cm depth (svm0-7); (b) total precipitation (Prec); (c) net radiation (Rn); (d) air temperature at 2m (T); (e) Vapor Pressure Deficit (VPD); (f) wind speed at 2m (U); (g) atmospheric pressure (P); (h) atmospheric CO_2 concentration; (i) Leaf Area Index (LAI).

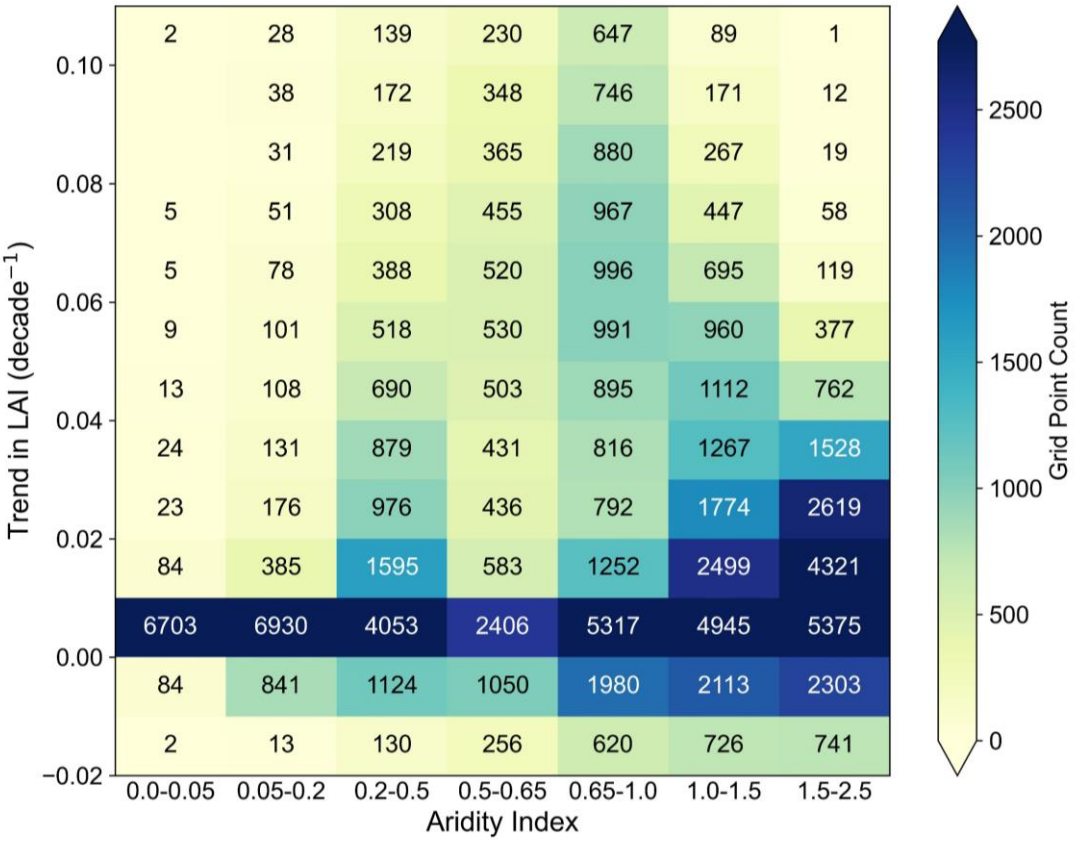

Figure S12. The number of grids in each bin grouped along the greening trend and aridity across mainland China.

Supplementary Tables

Table S1. Summary of the dataset applied in this study.

Role		Variable	Abbreviation	Unit	Source/Obtained Process	Spatial Resolution and Range	Temporal Resolution and Span
Compute ESI		Actual Evapotranspiration	ETa	mm	ERA5	0.1°, Global	Daily, 1950-2020
		Potential Evapotranspiration	ETp				
		ETp considering the CO_2 water-saving effect	$ETpPMCO_2$	mm	Calculated by Eq.(A4).		
As Influencing Factors	Water supply	Total Precipitation	Prec	mm	ERA5	0.1°, Global	Daily, 2001-2020
		Multi-layer Soil Moisture	svm0-7; svm7-28, svm28-100, svm100-289	$m^3 \cdot m^{-3}$			
		Root-zone Soil Moisture	Rsvm	$m^3 \cdot m^{-3}$	Calculated using Eq. Bx.		
	Energy Conditions	2m Air Temperature	T	°C	ERA5	0.1°, Global	Daily,2001-2020
		Net Radiation	Rn	$MJ \cdot m^{-2}$	Calculated by summing net solar radiation and net thermal radiation from ERA5.		
	Atmospheric Conditions	Atmospheric Pressure	P	kPa	ERA5	0.1°, Global	Daily, 2001-2020
		CO_2 Mole Fraction	CO_2	ppm	CT2022	3×2°, Global	3-hourly, 2001-2020
		2m Wind Speed	U	$m \cdot s^{-2}$	10m wind speed is calculated using the Pythagorean theorem with ERA5 10m u- and v-components of wind, then converted to 2m wind speed with the formula: $U = U_{10} * \frac{4.87}{\ln(67.8*10-5.42)}$.		
		Vapor Pressure Deficit	VPD	kPa	Calculated based on the Clausius-Clapeyron relation using 2m temperature and dew point temperature from ERA5 (Held and Soden, 2006; Zhong et al., 2023).		
	Vegetation Status	Leaf Area Index	LAI	$m^2 \cdot m^{-2}$	GLASS V60	500m, Global	8-day, 2001-2020
		Fractional Vegetation Cover	FVC	Dimensionless	GLASS V40		
		Normalized Difference Vegetation Index	NDVI	Dimensionless	MOD13C1	0.05°, Global	16-day, 2001-2020
		Enhanced Vegetation Index	EVI				
		kernel NDVI	kNDVI	Dimensionless	Calculated based on NDVI data using Eq.(2).		
Auxiliary Data		Aridity Index	AI	Dimensionless	Calculated by the ratio of annual Prec to ETp from the ERA5 dataset.		
		China Land Cover Dataset	-	-	Yang and Huang, (2021)	30m, China	Annual, 2001-2020
		Root Depth	-	mm	Stocker et al. (2023)	0.05°, Global	-

Table S2. Performance metrics for the RF and XGBoost regressor models.

It presents performance metrics (R^2, RMSE, MAE) of RF and XGBoost regressor models across 8-day, 16-day, and monthly temporal scales. Results are reported for both training and validation sets (70:30 split). Higher R^2 values (closer to 1) and lower RMSE/MAE values (approaching 0) indicate superior model performance. It reveals that XGBoost regressor model demonstrates higher accuracy than RF on the validation set, with a smaller accuracy discrepancy between the training and validation sets, thereby demonstrating superior generalization capability of the XGBoost model.

		8day				16day				Month			
		Training		Validation		Training		Validation		Training		Validation	
Classification	**Metrics**	**RF**	**XGBoost**	**RF**	**XGBoost**	**RF**	**XGBoost**	**RF**	**XGBoost**	**RF**	**XGBoost**	**RF**	**XGBoost**
Cropland	R^2	0.93	0.90	0.74	0.77	0.93	1	0.67	0.71	0.95	0.89	0.69	0.65
	RMSE	0	0.001	0.002	0.002	0	0	0.002	0.002	0	0	0.001	0.002
	MAE	0.017	0.022	0.034	0.032	0.013	0.003	0.034	0.032	0.010	0.017	0.028	0.029
Forest	R^2	0.93	0.93	0.67	0.74	0.92	0.86	0.63	0.62	0.93	0.98	0.45	0.51
	RMSE	0	0.001	0.004	0.003	0	0.001	0.002	0.002	0	0	0.002	0.002
	MAE	0.020	0.021	0.042	0.039	0.016	0.024	0.034	0.035	0.011	0.006	0.035	0.033
Grassland	R^2	0.93	0.98	0.63	0.66	0.92	0.83	0.59	0.59	0.93	1	0.54	0.58
	RMSE	0	0	0.001	0.001	0	0	0.001	0.001	0	0	0.001	0.001
	MAE	0.010	0.005	0.021	0.021	0.009	0.013	0.020	0.020	0.007	0.001	0.019	0.019
NonDryland	R^2	0.97	0.92	0.70	0.72	0.95	0.97	0.61	0.61	0.86	0.85	0.52	0.52
	RMSE	0	0	0.001	0.001	0	0	0.001	0.001	0	0	0.001	0.001
	MAE	0.011	0.015	0.028	0.027	0.009	0.006	0.023	0.023	0.010	0.011	0.021	0.021
Dryland	R^2	0.98	0.96	0.83	0.85	0.97	1	0.80	0.84	0.97	1	0.70	0.69
	RMSE	0	0	0	0	0	0	0	0	0	0	0	0
	MAE	0.006	0.009	0.018	0.016	0.006	0.003	0.016	0.015	0.006	0	0.017	0.017
SemiHumid	R^2	0.95	0.93	0.74	0.75	0.95	0.94	0.73	0.73	0.96	0.86	0.60	0.64
	RMSE	0	0	0.001	0.001	0	0	0.001	0.001	0	0	0.001	0.001
	MAE	0.012	0.015	0.026	0.026	0.011	0.012	0.026	0.026	0.008	0.015	0.023	0.023
SemiArid	R^2	0.97	0.98	0.80	0.82	0.96	0.99	0.79	0.81	0.96	0.98	0.56	0.66
	RMSE	0	0	0.001	0.001	0	0	0.001	0.001	0	0	0.001	0.001
	MAE	0.010	0.007	0.025	0.024	0.011	0.005	0.025	0.023	0.008	0.006	0.028	0.025
Arid	R^2	0.98	0.97	0.92	0.92	0.93	0.98	0.80	0.84	0.98	0.99	0.80	0.82
	RMSE	0	0	0	0	0	0	0	0	0	0	0	0
	MAE	0.005	0.007	0.011	0.011	0.007	0.005	0.014	0.013	0.004	0.003	0.011	0.011

Table S3. Performance metrics for the XGBoost regression model after variable pre-screening.

The input variables for parameter sets in the table were configured as follows:
- R0: svm0-7, Rn, T, VPD, U, P, CO_2, and LAI
- R1: replaced svm0-7 with Prec while retaining all other variables from R0

		8day		16day		month	
Classification	**Metrics**	**Training**	**Validation**	**Training**	**Validation**	**Training**	**Validation**
R0	R^2	0.82	0.64	0.85	0.62	0.86	0.62
	RMSE	0	0.001	0	0.001	0	0
	MAE	0.017	0.023	0.012	0.019	0.009	0.015
R1	R^2	0.82	0.65	0.93	0.58	0.85	0.52
	RMSE	0	0.001	0	0.001	0	0.001
	MAE	0.018	0.024	0.009	0.021	0.010	0.018

Table S4. List of Variance Inflation Factor.

For each grid, collinearity tests were conducted on the anomaly series of variables across three temporal scales. The table lists the average values of the VIF (Variance Inflation Factor) for all grids, along with the 5th percentile (superscript) and the 95th percentile (subscript). Two scenarios, R0 and R1, have been established based on different combinations of input parameters to isolate and contrast the effects of soil moisture and precipitation.

Parameter Set: R0

Temporal resolution	svm0-7	Rn	T	VPD	U	P	CO_2	LAI
8day	$1.59_{2.14}^{1.20}$	$2.04_{3.18}^{1.09}$	$2.10_{3.32}^{1.34}$	$2.85_{4.15}^{1.87}$	$1.37_{2.03}^{1.06}$	$1.43_{1.98}^{1.07}$	$1.01_{1.02}^{1.00}$	$1.08_{1.23}^{1.01}$
16day	$1.64_{2.30}^{1.20}$	$2.05_{3.19}^{1.11}$	$2.14_{3.40}^{1.33}$	$3.00_{4.65}^{1.84}$	$1.43_{2.25}^{1.07}$	$1.40_{1.90}^{1.07}$	$1.01_{1.03}^{1.00}$	$1.11_{1.30}^{1.02}$
month	$1.67_{2.41}^{1.19}$	$2.09_{3.35}^{1.15}$	$2.27_{3.87}^{1.35}$	$3.16_{5.21}^{1.84}$	$1.54_{2.60}^{1.09}$	$1.42_{1.89}^{1.07}$	$1.01_{1.04}^{1.00}$	$1.15_{1.39}^{1.03}$

Parameter Set: R1

Temporal resolution	Prec	Rn	T	VPD	U	P	CO_2	LAI
8day	$1.85_{2.64}^{1.45}$	$2.30_{3.53}^{1.21}$	$2.28_{3.69}^{1.37}$	$2.96_{4.72}^{1.95}$	$1.38_{2.05}^{1.06}$	$1.01_{1.02}^{1.00}$	$1.45_{2.00}^{1.09}$	$1.05_{1.16}^{1.01}$
16day	$1.98_{3.01}^{1.49}$	$2.31_{3.54}^{1.18}$	$2.37_{4.28}^{1.37}$	$3.23_{5.73}^{1.99}$	$1.44_{2.28}^{1.07}$	$1.01_{1.02}^{1.00}$	$1.42_{1.92}^{1.09}$	$1.08_{1.24}^{1.01}$
month	$2.07_{3.32}^{1.46}$	$2.28_{3.60}^{1.17}$	$2.52_{5.13}^{1.37}$	$3.59_{6.73}^{2.09}$	$1.54_{2.62}^{1.09}$	$1.01_{1.03}^{1.00}$	$1.44_{1.92}^{1.08}$	$1.12_{1.35}^{1.02}$

Table S5. Interpretation of sensitivity obtained from Memory Dynamic Linear Model.

Absolute values of θ depict the evapotranspiration stress resistance to anomalies in each variable. Large absolute values indicate strong evapotranspiration stress responses to corresponding variable anomalies.

Classify	Description	Sign
Water-related Factors	θ_{svm}	*Positive* - Wetter conditions than average induce positive ESI anomalies, meaning that evaporative stress is alleviated.
	θ_{Prec}	
Vegetation-related Factors	θ_{LAI}	*Positive* - Denser and healthier vegetation conditions than average induce positive ESI anomalies, meaning that evaporative stress is alleviated.
Energy-related Factors	θ_{Rn}	*Negative* - Above-average thermal conditions induce negative ESI anomalies, meaning that evaporative stress is aggravated.
	θ_{T}	
Atmosphere-related Factors	θ_{U}	*Positive* - Faster wind speeds than average induce positive ESI anomalies, meaning that evaporative stress is alleviated.
	θ_{VPD}	*Negative* - More deficient atmospheric vapor pressure than average induce negative ESI anomalies, meaning that evaporative stress is aggravated.
	θ_{P}	*Negative* - Higher atmospheric pressure than average induce negative ESI anomalies, meaning that evaporative stress is aggravated.
	θ_{CO2}	*Negative* - Higher CO_2 concentration than average induce negative ESI anomalies, meaning that evaporative stress is aggravated.

Table S6. Site characteristics of Eddy Covariance Flux Tower.

No.	Site Name	Lon (°E)	Lat (°N)	Vegetation Type (IGBP)	Altitude (m)	Duration	Source	Residual Energy (W/m^2)	Reference
1	CBF	128.10	42.40	DBF	2180m	2003.01-2010.12	ChinaFlux	21.50	(Yu et al., 2006, 2008, 2014)
2	DXG	91.08	30.85	GRA	4400m	2004.01-2010.12		-15.65	
3	DHF	112.53	23.17	MF		2003.01-2010.12		15.90	
4	HBGS	101.33	37.67	GRA	3400m	2003.01-2010.12		2.09	
5	NMG	116.40	43.33	GRA		2004.01-2010.12		9.85	
6	QYF	115.07	26.73	ENF		2003.01-2010.12		15.14	
7	YCA	116.57	36.83	CRO	30m	2003.01-2010.12		6.46	
8	BNXF	101.27	21.90	CVM		2010.07-2014.12		23.85	(Yu et al., 2021)
9	HZF	121.02	51.78	DNF	773m	2014.01-2018.12		34.45	(Yan et al., 2023)
10	XLG	116.67	43.55	GRA	1250m	2006.01-2015.12		8.76	(Wang et al., 2023)
11	ALF	101.03	24.54	EBF	2400-2600m	2009.01-2013.12		12.20	(Qi et al., 2021)
12	ZOG	102.55	32.80	GRA	3500m	2015.06-2020.12		18.63	(Chen et al., 2023)
13	CLC	123.47	44.60	CRO	143	2018.06-2020.12		16.47	(Dong et al., 2023)
14	CN-Du2	116.28	42.05	GRA	1324m	2006.01-2008.12	FLUXNET	6.11	(Chen et al., 2009; Pastorello et al., 2020)
15	CN-Cng	123.50	44.58	GRA	171m	2007.01-2010.12		-0.60	(Pastorello et al., 2020)
16	CN-Du3	116.28	42.06	GRA	1324m	2009.01-2010.12		19.73	
17	CN-Sw2	111.90	41.79	GRA	1456m	2010.01-2012.12		12.96	
18	DZF	109.48	19.55	EBF	144m	2010.01-2018.12	Chinese Academy of Tropical Agricultural Sciences (CATAS)	22.74	(Yang et al., 2022)
19	WSC	116.05	36.65	CRO	30m	2005.05-2006.09	(Tsinghua University) THU	13.26	(Lei and Yang, 2010a, b)
20	DSG	98.94	38.84	GRA	3739m	2015.01-2017.12	HiWATER	-42.08	

21	EJB	100.24	38.01	BSV	1054m	2015.06-2017.09		3.82	(Che et al., 2019; Liu et al., 2011, 2016, 2018, 2023)
22	HZB	100.32	38.76	BSV	1731m	2018.01-2020.12		-8.16	
23	EJM	101.13	41.99	MF	874m	2013.08-2017.12		-1.13	
24	JYG	101.11	37.84	GRA	3750m	2018.08-2020.12		4.38	
25	XYG	101.86	37.56	GRA	3616m	2019.04-2020.12	Cold and Arid Research Network of Lanzhou university (CARN)	10.79	(Changming Zhao and Renyi Zhang, 2021)
26	MQB	103.67	39.21	BSV	1020m	2019.08-2020.12		31.06	

According to the International Geosphere-Biosphere Programme (IGBP) classification, BSV = Barren Sparse Vegetation, CRO = Croplands, CVM = Cropland/Natural Vegetation Mosaics, DBF = Deciduous Broadleaf Forests, DNF = Deciduous Needleleaf Forests, EBF = Evergreen Broadleaf Forests, ENF = Evergreen Needleleaf Forests, GRA = Grasslands, MF = Mixed Forests, WET = Permanent Wetlands

References

Changming Zhao and Renyi Zhang: Cold and Arid Research Network of Lanzhou university (eddy covariance system of Guazhou station, 2020), https://doi.org/10.11888/Meteoro.tpdc.271477, 2021.

Che, T., Li, X., Liu, S., Li, H., Xu, Z., Tan, J., Zhang, Y., Ren, Z., Xiao, L., Deng, J., Jin, R., Ma, M., Wang, J., and Yang, X.: Integrated hydrometeorological, snow and frozen-ground observations in the alpine region of the Heihe River Basin, China, Earth Syst. Sci. Data, 11, 1483–1499, https://doi.org/10.5194/essd-11-1483-2019, 2019.

Chen, S., Chen, J., Lin, G., Zhang, W., Miao, H., Wei, L., Huang, J., and Han, X.: Energy balance and partition in Inner Mongolia steppe ecosystems with different land use types, Agricultural and Forest Meteorology, 149, 1800–1809, https://doi.org/10.1016/j.agrformet.2009.06.009, 2009.

Chen, W., Wang, S., and Niu, S.: A dataset of carbon, water and heat fluxes of Zoige alpine meadow from 2015 to 2020, China Scientific Data, 8, https://doi.org/10.11922/11-6035.csd.2023.0009.zh, 2023.

Dong, G., Wang, Y., Wang, K., Jiang, S., and Shao, C.: A dataset of carbon and water fluxes in the Changling alkali-saline paddy rice fields in the Songnen Plain, China (2018 –2020), China Scientific Data, 2023.

Lei, H. and Yang, D.: Interannual and seasonal variability in evapotranspiration and energy partitioning over an irrigated cropland in the North China Plain, Agricultural and Forest Meteorology, 150, 581–589, https://doi.org/10.1016/j.agrformet.2010.01.022, 2010a.

Lei, H. and Yang, D.: Seasonal and interannual variations in carbon dioxide exchange over a cropland in the North China Plain, Global Change Biology, 16, 2944–2957, https://doi.org/10.1111/j.1365-2486.2009.02136.x, 2010b.

Liu, S., Xu, Z. W., Wang, W. Z., Jia, Z. Z., Zhu, M. J., Bai, J., and Wang, J. M.: A comparison of eddy-covariance and large aperture scintillometer measurements with respect to the energy balance closure problem, Hydrol. Earth Syst. Sci., 15, 1291–1306, https://doi.org/10.5194/hess-15-1291-2011, 2011.

Liu, S., Xu, Z., Song, L., Zhao, Q., Ge, Y., Xu, T., Ma, Y., Zhu, Z., Jia, Z., and Zhang, F.: Upscaling evapotranspiration measurements from multi-site to the satellite pixel scale over heterogeneous land surfaces, Agricultural and Forest Meteorology, 230–231, 97–113, https://doi.org/10.1016/j.agrformet.2016.04.008, 2016.

Liu, S., Li, X., Xu, Z., Che, T., Xiao, Q., Ma, M., Liu, Q., Jin, R., Guo, J., Wang, L., Wang, W., Qi, Y., Li, H., Xu, T., Ran, Y., Hu, X., Shi, S., Zhu, Z., Tan, J., Zhang, Y., and Ren, Z.: The Heihe Integrated Observatory Network: A Basin-Scale Land Surface Processes Observatory in China, Vadose Zone Journal, 17, 1–21, https://doi.org/10.2136/vzj2018.04.0072, 2018.

Liu, S., Xu, Z., Che, T., Li, X., Xu, T., Ren, Z., Zhang, Y., Tan, J., Song, L., Zhou, J., Zhu, Z., Yang, X., Liu, R., and Ma, Y.: A dataset of energy, water vapor, and carbon exchange observations in oasis–desert areas from 2012 to 2021 in a typical endorheic basin, Earth Syst. Sci. Data, 15, 4959–4981, https://doi.org/10.5194/essd-15-4959-2023, 2023.

Pastorello, G., Trotta, C., Canfora, E., Chu, H., Christianson, D., Cheah, Y.-W., Poindexter, C., Chen, J., Elbashandy, A., Humphrey, M., Isaac, P., Polidori, D., Reichstein, M., Ribeca, A., Van Ingen, C., Vuichard, N., Zhang, L., Amiro, B., Ammann, C., Arain, M. A., Ardö, J., Arkebauer, T., Arndt, S. K., Arriga, N., Aubinet, M., Aurela, M., Baldocchi, D., Barr, A., Beamesderfer, E., Marchesini, L. B., Bergeron, O., Beringer, J., Bernhofer, C., Berveiller, D., Billesbach, D., Black, T. A., Blanken, P. D., Bohrer, G., Boike, J., Bolstad, P. V., Bonal, D., Bonnefond, J.-M., Bowling, D. R., Bracho, R., Brodeur, J.,

Brümmer, C., Buchmann, N., Burban, B., Burns, S. P., Buysse, P., Cale, P., Cavagna, M., Cellier, P., Chen, S., Chini, I., Christensen, T. R., Cleverly, J., Collalti, A., Consalvo, C., Cook, B. D., Cook, D., Coursolle, C., Cremonese, E., Curtis, P. S., D'Andrea, E., Da Rocha, H., Dai, X., Davis, K. J., Cinti, B. D., Grandcourt, A. D., Ligne, A. D., De Oliveira, R. C., Delpierre, N., Desai, A. R., Di Bella, C. M., Tommasi, P. D., Dolman, H., Domingo, F., Dong, G., Dore, S., Duce, P., Dufrêne, E., Dunn, A., Dušek, J., Eamus, D., Eichelmann, U., ElKhidir, H. A. M., Eugster, W., Ewenz, C. M., Ewers, B., Famulari, D., Fares, S., Feigenwinter, I., Feitz, A., Fensholt, R., Filippa, G., Fischer, M., Frank, J., Galvagno, M., et al.: The FLUXNET2015 dataset and the ONEFlux processing pipeline for eddy covariance data, Sci Data, 7, 225, https://doi.org/10.1038/s41597-020-0534-3, 2020.

Qi, D., FEI, X., SONG, Q., ZHANG, Y., SHA, L., LIU, Y., ZHOU, W., LU, Z., and FAN, Z.: A dataset of carbon and water fluxes observation in subtropical evergreen broad-leaved forest in Ailao Shan from 2009 to 2013, China Scientific Data, 6, https://doi.org/10.11922/csdata.2020.0089.zh, 2021.

Simoen, E., Papadimitriou, C., and Lombaert, G.: On prediction error correlation in Bayesian model updating, Journal of Sound and Vibration, 332, 4136–4152, https://doi.org/10.1016/j.jsv.2013.03.019, 2013.

Wang, Y., You, C., and Chen, S.: A dataset of carbon and water fluxes of mowing grasslands in Xilinhot, Inner Mongolia during 2006-2015, China Scientific Data, 2023.

Yan, Y., Zhou, G., Jia, B., Song, J., and Zhang, S.: A dataset of carbon and water fluxes of the boreal forest ecosystem in Huzhong (2014 – 2018), China Scientific Data, 2023.

Yang, S., Liu, J., Yang, C., Lan, G., Song, B., and Wu, Z.: A dataset of carbon and water fluxes and micrometerological elements in Danzhou rubber plantation (2010-2018), China Scientific Data, 2022.

Yu, G., Wen, X.-F., Sun, X.-M., Tanner, B. D., Lee, X., and Chen, J.-Y.: Overview of ChinaFLUX and evaluation of its eddy covariance measurement, Agricultural and Forest Meteorology, 137, 125–137, https://doi.org/10.1016/j.agrformet.2006.02.011, 2006.

Yu, G., Zhang, L., Sun, X., Fu, Y., Wen, X., Wang, Q., Li, S., Ren, C., Song, X., Liu, Y., Han, S., and Yan, J.: Environmental controls over carbon exchange of three forest ecosystems in eastern China, Global Change Biology, 14, 2555–2571, https://doi.org/10.1111/j.1365-2486.2008.01663.x, 2008.

Yu, G., Chen, Z., Piao, S., Peng, C., Ciais, P., Wang, Q., Li, X., and Zhu, X.: High carbon dioxide uptake by subtropical forest ecosystems in the East Asian monsoon region, Proc. Natl. Acad. Sci. U.S.A., 111, 4910–4915, https://doi.org/10.1073/pnas.1317065111, 2014.

Yu, H., QI, D., ZHANG, Y., SHA, L., LIU, Y., ZHOU, W., DENG, Y., and SONG, Q.: An observation dataset of carbon and water fluxes in Xishuangbanna rubber plantations from 2010 to 2014, China Scientific Data, 6, https://doi.org/10.11922/csdata.2020.0090.zh, 2021.

Zhang, E. L., Feissel, P., and Antoni, J.: A comprehensive Bayesian approach for model updating and quantification of modeling errors, Probabilistic Engineering Mechanics, 26, 550–560, https://doi.org/10.1016/j.probengmech.2011.07.001, 2011.